Microring resonator-coupled photoluminescence from silicon W centers

IOP Publishing J. Phys. Photonics 2 (2020) 045001 https://doi.org/10.1088/2515-7647/ab95f2

Journal of Physics: Photonics

OPEN ACCESS

RECEIVED
10 January 2020

REVISED
28 March 2020

ACCEPTED FOR PUBLICATION
22 May 2020

PUBLISHED
10 July 2020

PAPER

Microring resonator-coupled photoluminescence from silicon W centers

A N Tait[1], S M Buckley[1], J Chiles[1], A N McCaughan[1], S Olson[2], S Papa Rao[2,3], S W Nam[1], R P Mirin[1] and J M Shainline[1]

[1] Applied Physics Division, National Institute of Standards and Technology, Boulder, CO 80305, United States of America
[2] NY CREATES, Albany, NY 12203, United States of America
[3] SUNY Polytechnic Institute, Albany, NY 12203, United States of America

E-mail: alexander.tait@nist.gov

Keywords: silicon light sources, microresonators, photoluminescence, cryogenic photonics, silicon waveguides

Abstract

Silicon defect centers are promising candidates for waveguide-integrated silicon light sources. We demonstrate microresonator- and waveguide-coupled photoluminescence from silicon W centers. Microphotoluminescence measurements indicate wavelengths on-resonance with resonator modes are preferentially coupled to an adjacent waveguide. Quality factors of at least 5,300 are measured, and free spectral ranges closely match expectation. The W center phonon sideband can be used as a spectral diagnostic for a broader range of waveguide-based devices on cryogenic silicon photonic platforms.

1. Introduction

The rapid growth of the silicon photonics industry has the potential to bring photonic manufacturing economies comparable to those of the silicon microelectronics industry. In addition to potentials for large-volume production, silicon photonics opens possibilities for large-scale photonic processing architectures that could not be conceived of in fiber or III-V platforms [1–3]. In all photonic systems, light sources are required. Silicon does not readily emit light at room temperature due to its indirect bandgap. Therefore, most efforts in silicon photonics use external light sources coupled to chip with fiber. The use of external light sources presents critical burdens of fiber packaging, resulting in severe scaling limitations.

Substantial research has been dedicated to developing integrated light sources for silicon photonics [4, 5]. Each approach has advantages and drawbacks. These include rare earth element doping (low brightness), wafer bonding of III-V quantum wells [6] (challenging and expensive processing), epitaxial growth of III-V quantum dots [7] (specialized epitaxy steps), and strain engineering of germanium [8] (fragility and low yield). All of these approaches with the exception of germanium involve the introduction of materials that are incompatible with typical silicon foundries.

Silicon emitters can be realized by creating specific defects in the silicon crystal. Emissive defect centers in silicon have been studied for seven decades, reviewed in [9, 10], but they have not demonstrated utility as sources for silicon photonic circuits in key applications of interest. Their application domains are limited by a requirement of low-temperature operation; however, this is a limitation of little consequence when cryogenic operation is acceptable or required. Defect centers possess several important advantages, most crucial of which is their ease of fabrication: local modifications to the native crystal as opposed to the introduction of new materials and/or structures. If monolithically integrated with waveguides, defect center light sources could provide a compact, inexpensive, scalable solution for superconducting optoelectronic neural networks [2] and optical quantum information systems. In optical quantum information systems, the complex photonic circuitry can operate at room temperature, but then off-chip cryogenic single-photon detectors are needed anyways [11, 12]. The prospect of monolithic sources and single-photon detectors could potentially justify the overhead of cooling the entire quantum system.

In this work, we explore the coupling of W-center photoluminescence to silicon-on-insulator waveguides and microring resonators, a platform shown in figure 1. W centers are trigonal defects that have a

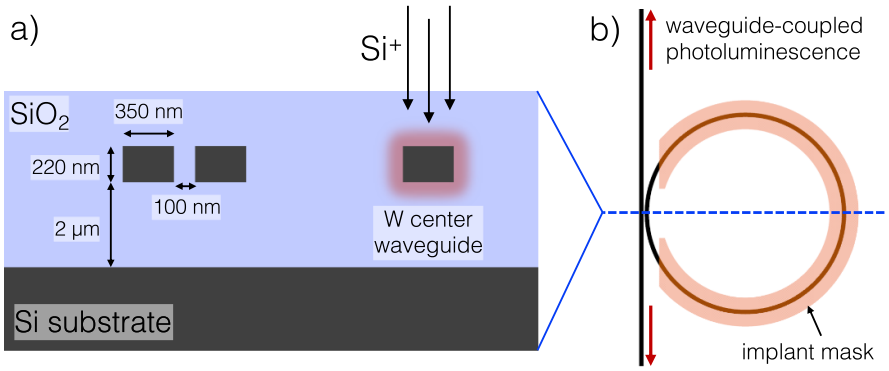

Figure 1. Illustration of platform and devices. (a) Waveguide cross-sections. All waveguides are designed to be 220 nm thick and 350 nm wide such that they are single mode at 1218 nm. As fabricated, waveguide widths were 390 nm. W-center emitters are created by implanting a waveguide with silicon ions and annealing. Evanescent couplers between microrings and the bus waveguide have 100 nm gaps in this work. (b) Top view of microring resonator coupled to a waveguide. Black is silicon; red is the pattern of ion implants defined lithographically; blue, dashed line is the cross-section slice. Implant regions are widened to relax alignment tolerance. Ions that miss the silicon become embedded in the buried oxide and have no effect on the studied devices.

zero-phonon line at 1218 nm and phonon sideband over 1225 nm–1275 nm [13]. They are created by implanting silicon crystal with silicon ions. We report that photoluminescence emitted into resonator modes preferentially couples to a bus waveguide, resulting in spectra with periodic resonances that are characteristic of microrings. The free spectral ranges of different devices closely match with theoretical models, thus allowing extraction of the group velocity parameter with a $R^2 = 0.991$ coefficient of determination. We record resonances with quality factors up to 5,300. Infrared camera and polarization measurements are used to confirm correct operation of the experimental technique for differentiating waveguide-coupled from free-space-coupled photoluminescence.

In prior work, W center waveguide coupling has been achieved in an electrically pumped device whose total power output was measured by an on-chip detector [14]. While the current work aims to support development of electrically pumped devices, micro-photoluminescence (PL) measurements offer additional research opportunities and richer information than electrical devices alone, such as pumping an array of devices or resolving emission spectra. In prior micro-PL measurements of defect centers in silicon-on-insulator, waveguides were not investigated, although several of these devices were on silicon-on-insulator of dimensions that could potentially support waveguides [15–17]. Other studies have shown coupling of various defect centers to suspended microdisk [18] and photonic crystal [19, 20] cavities; however, PL collection has always occurred directly above the structure being pumped, i.e. normal to the surface of the sample.

We monitor waveguide-coupled luminescence unambiguously by collecting from a grating coupler that is spatially offset from the microring being pumped. This circuit is shown in figure 2. The experimental apparatus for collecting offset photoluminescence is similar to those used in prior research on quantum dots and photonic crystals [21–23]. In contrast to those works, both the resonator under study and the offsetting circuitry itself are based on oxide-clad, single-mode silicon rib waveguides of the same type that form the basis of mainstream silicon photonic platforms. Results imply a potential to integrate W centers in more complex photonic integrated circuits and an ability to generalize the experimental technique to the study of a wide range of more complex photonic circuits with embedded emissive defect centers.

2. Layout and fabrication

The substrate used for this study was a 76 mm silicon-on-insulator (SOI) wafer with a 220 nm silicon device layer on a 2 μm buried oxide. Implants were masked by 600 nm thick positive-tone resist patterned by electron-beam lithography. The wafer was then implanted with Si ions at a commercial facility. The silicon etch pattern was masked by an electron-beam-patterned oxide hard mask. The 220 nm thick device layer was fully etched to the buried oxide with a reactive ion etch based on SF_6 and C_4F_8. Finally, the wafer was encapsulated by a 1.5 μm oxide. The wafer was diced into 1 cm $\times$ 1 cm die, which were then annealed. Implant and anneal conditions were chosen to yield the optimum W-center brightness as determined in reference [17].

Waveguides were designed to be 350 nm wide such that they are single-mode at 1220 nm. Scanning electron micrographs of the waveguides showed an actual width of 390 nm. Comparisons of insertion loss in single-mode waveguides of different lengths indicated a waveguide loss of 18 dB cm^{-1}, which is significantly

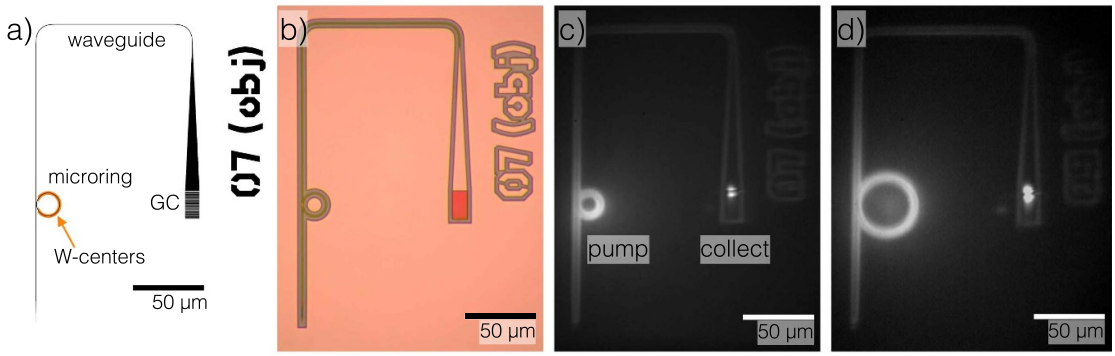

Figure 2. Different views of the circuit for offset collection from a microring resonator (MRR) with radius $r = 8$ μm. (a) Design layout. Silicon is black and the location of W-center implants is orange. GC: grating coupler. (b) Visible microscope image of the fabricated circuit. (c) Infrared image of the circuit when the MRR is optically pumped. Photoluminescence is observed directly from the MRR (free-space-coupled) and also from the offset grating coupler (waveguide-coupled). (d) Infrared image of a different device with larger radius, $r = 20$ μm.

higher than expected due to a non-optimized etch recipe. The peak brightness of the W-center zero phonon line (ZPL) in an unpatterned SOI region was measured to give 4,400 $\pm$ 220 counts/s with a 300 μW pump, which agrees with different cooldowns of different samples on the same setup. Microrings were designed with coupling gaps of 100 nm and radii of $r(\mu\text{m}) = [2, 4, 8, 10, 20, 30]$.

We employ a waveguide-based offset collection technique that allows for observation of waveguide-coupled PL, which was introduced in our recent conference proceeding [24]. The silicon photonic circuit, shown in figure 2, spatially separates waveguide-coupled PL from free-space-coupled PL, and the optical apparatus isolates these two collection points. In the circuit, an MRR implanted with W centers is evanescently coupled to a bus waveguide. When the MRR is pumped, some component of the PL is emitted upward into free-space. Another component of the PL is emitted into the resonator modes. Light in the resonator modes couples to the bus waveguide and is then routed to the spatially offset grating coupler (GC). The GC is designed to emit normal to the surface and is located 100 μm away from the center of the MRR.

3. Experimental Apparatus

A simplified experimental setup is shown in figures 3(a) and (b) and in more detail in the Supplementary Information. The primary components are a pump, cryostat, objective, and infrared (IR) spectrometer. The 11 mW laser pump at 635 nm (red) is focused onto the device in the cryostat. Excited electrons undergo an optical transition in the W centers, emitting IR photoluminescence in the infrared (depicted as blue). This PL is directed to a spectrometer and InGaAs camera. PL is emitted from two locations: the device itself and the offset GC. When the PL is imaged with a lens, the two emission sources are spatially separated. These distinct emission sources are seen in figure 3(c).

The objective performs both roles of focusing the pump to a spot and collecting the PL through a window in the cryostat. The infinity corrected, long working distance objective has 10$\times$ magnification and a numerical aperture of 0.42. The sample was fixed, and the objective was mounted on XYZ translation stages. Three mirrors were mounted to the stages in a periscope configuration that maintains a consistent relationship between beams on the optical table and the objective, despite the movement of the objective. A visible camera was used to navigate the sample and position the pump spot. More detail on visible microscopy, motion control, spot size control, and IR imaging can be found in the Supplementary Information section.

The procedure for discerning waveguide-coupled PL with this setup is as follows. Initially, the setup was aligned by collecting the free-space-coupled PL from an unpatterned, implanted region. The pump was positioned over an implanted MRR and fine adjusted such as to maximize the free-space-coupled emission signal from the MRR. Then, a razor blade in an image plane is moved to block the center of the field of view, seen in figure 3(d). The blade is translated by a further 500 μm corresponding to 50 μm on chip. Figure 3(b) shows the beams when in the blocking configuration, and figure 3(e) shows the corresponding IR image. Once the center is blocked, mirrors before the spectrometer are adjusted to optimize the offset signal. In this blocking configuration, only the offset PL from the grating coupler is observed.

The optical cryostat is based on a modified cryopump. The top flange of the cryopump chamber was removed, and a machined brass post and brass sample holder were attached to the 15 K stage of the cold

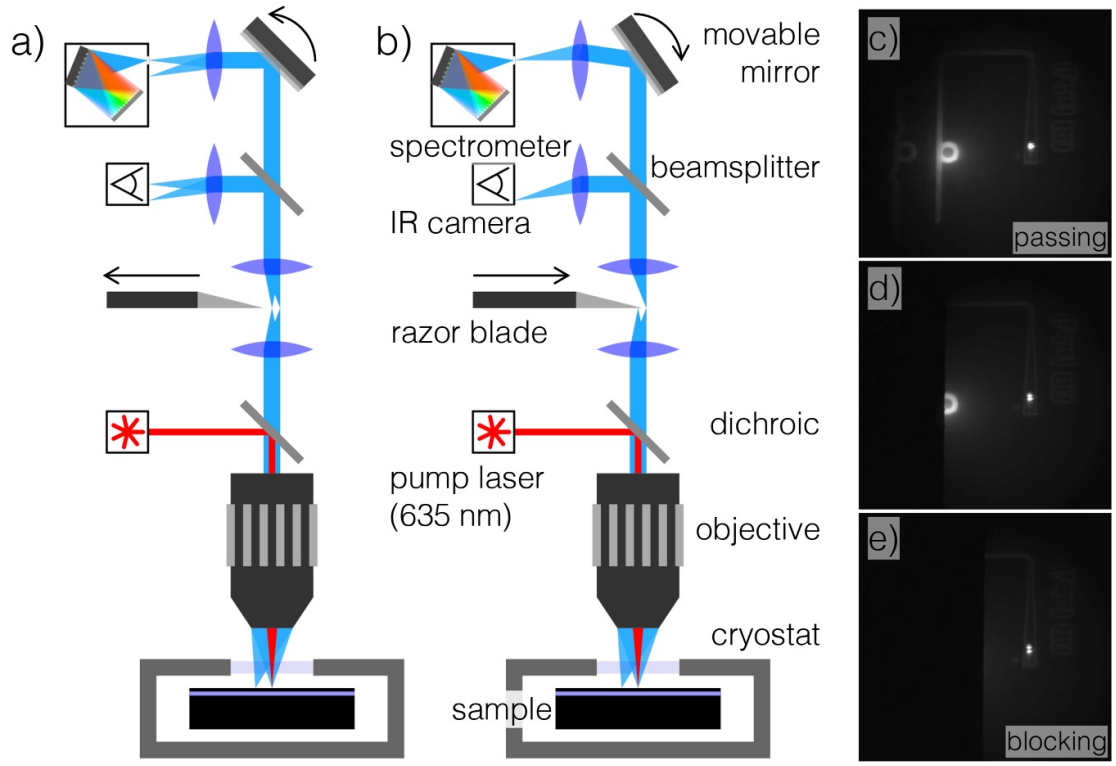

Figure 3. Simplified experimental diagram and visualization of the center PL blocking technique. The configuration can be non-blocking (a) or blocking (b). A pump laser (red) is focused onto a W-center device. Infrared (IR) PL is collected by the same objective. The returning PL transmits through a dichroic mirror and a razor blade assembly. Then the PL is split to an IR camera and spectrometer. When the central PL is blocked, the mirrors preceding the spectrometer are adjusted such that the offset component enters the slit of the spectrometer. (c-e) Verification of the razor blade technique for isolating offset PL. (c) Razor non-blocking corresponding to (a); (d) razor halfway across MRR; (e) razor fully blocking, corresponding to (b). Data is collected in the blocking state.

head. A radiation shield canister with a window was attached to the 80 K stage. Lastly, a new top flange with a window was put in place to seal the vacuum chamber. The cold head is driven by a closed-cycle helium compressor. A silicon diode thermometer is attached to the bottom of the sample holder and read a minimum temperature of 19.8 K. The cryopump motor causes substantial vibration, meaning that optical measurements of small devices cannot be taken while it is running. We estimated a sample vibration displacement between 50 and 100 μm. We addressed this vibration problem by turning the compressor off during fine alignment and measurement. While it is off, the temperature begins to increase, reaching 40 K in approximately 12 minutes. W-center brightness drops by 12% between 28 K and 40 K and then drops off precipitously above 45 K [13, 17]. All measurements in this work were taken between 28 K and 40 K.

4. Results

Waveguide-coupled spectra from MRRs with six different radii are shown in figure 4. These spectra (red) are compared to that of the control region (blue), which was an unpatterned, implanted SOI region. Emission at the zero phonon line (ZPL) at 1218 nm is 21-times brighter than the peak of the sideband; however, the sideband emission integrated over 1225 nm–1275 nm accounted for 55% of the total emission. In this measurement, the sideband was 20 dB above background noise, allowing us to spectrally resolve emission and transmission spectra over a broad, 50 nm wavelength range. It therefore can be used as a diagnostic technique for a wide range of cryogenic silicon photonic devices.

The collected PL is brighter at wavelengths that resonate with the microresonator and nearly undetectable off-resonance. This result indicates that only the PL emitted into the resonant modes couples to the bus waveguide. Preferential waveguide coupling does not necessarily mean preferential emission into the resonant modes, as in the sense of stimulated emission or Purcell enhancement, of which we did not observe conclusive evidence. The shape of the envelope of the peaks closely follows that of the W-center sideband from the control region. This indicates that the wavelength dependence of evanescent couplers and GC are relatively flat over the window. The data are not normalized, and it is coincidental that the amplitudes (dependent on multiple unmeasured factors, discussed below) also match. In figure 4(f), the peak

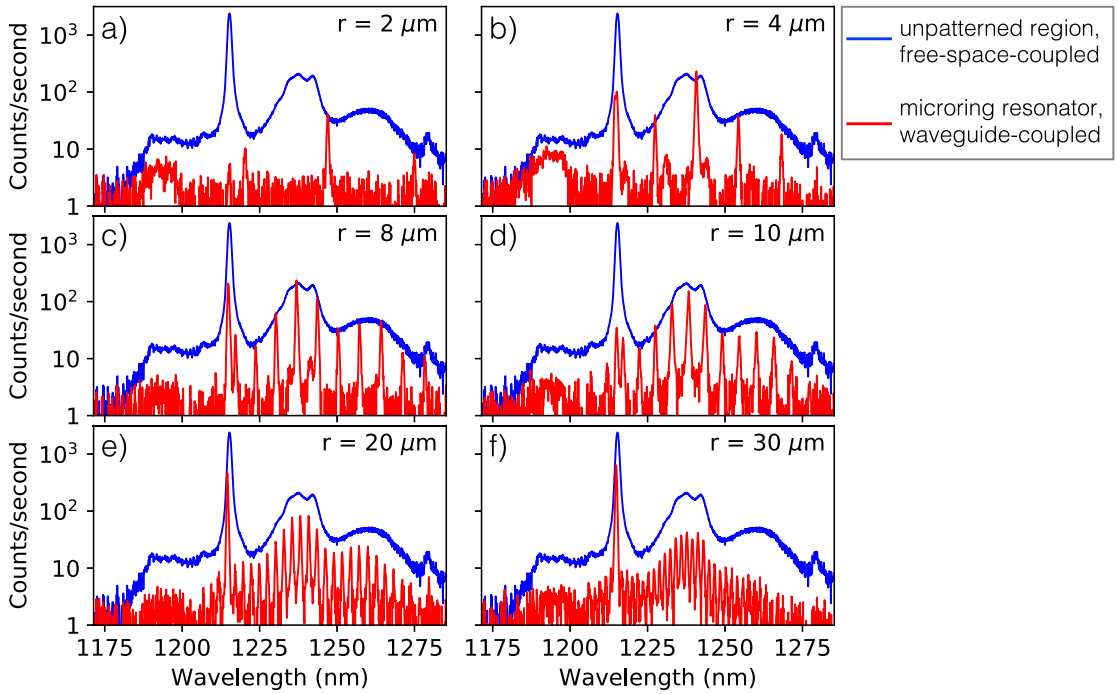

Figure 4. Comparison of free-space-coupled PL from an unpatterned control region (blue curves) to waveguide-coupled PL from the GCs connected to MRRs of different radii (red curves). Multiple peaks at evenly spaced frequencies are indicative of multiple MRR resonances. As MRR radius increases, the free spectral range decreases. The zero phonon line amplitude depends on where its wavelength falls relative to a resonator mode.

amplitudes are significantly weaker because the MRR diameter was much larger than the focused pump spot. The pump was defocused so that more of it reaches the MRR waveguide; however, most of the pump power still passed through the unimplanted center of the largest MRRs.

The zero phonon line was visible in every sample, but its amplitude varied considerably. Its amplitude depends on how close a MRR resonance falls to 1218 nm. As a result of resonance sensitivity to fabrication variation, it is difficult to control the absolute resonant wavelengths [25]. On the other hand, the relative spacing between resonances, i.e. free spectral range (FSR), is precisely determined by MRR radius according to the formula

$$\mathrm{FSR} = \frac{\lambda^2}{2\pi r \cdot n_g}, \tag{1}$$

where n_g is the group index, and λ is wavelength. The best fit of the measured FSRs from figure 4 in the 1225 nm–1250 nm range yields $n_g = 4.51$ with a fit residual of $R^2 = 0.991$, meaning that there is close agreement between this model and the data. Previous measurements of similar MRRs, taken using a transmission spectrum analyzer and fiber alignment setup, yielded a group index of 4.33 ± 0.03; however, that measurement was at room temperature and without W centers.

Figure 5(a) shows a high resolution waveguide-coupled spectrum of the $r = 8$ μm MRR. A spectrometer grating with 1,200 grooves mm^{-1} was used for this measurement compared to the spectrometer grating used for figure 4 with 300 grooves mm^{-1}. The full-width half-maximum (FWHM) of the center peak was measured to be $\Delta\lambda = 0.23$ nm, which is near the resolution limit of the detector array. The quality factor of this feature is 5,300. Since any kind of misalignment or defocus can affect the actual resolution limit, it is possible that this Q factor is underestimated. The intrinsic Q of this MRR was at most 55,000 due to waveguide propagation loss. The extrinsic Q is determined by the combined round trip propagation loss plus ring-to-waveguide coupling coefficient, which was simulated to be $\kappa^2 = 0.121$. The extrinsic Q is therefore expected to be at most 7,700. Measurement and simulation place relatively tight bounds on the actual extrinsic Q between 5,300–7,700. In [24], measurements of a microdisk on the same setup and sample found resonances with Q factors up to 7,160. The higher Q in that work can be explained because higher-radial-order microdisk modes couple more weakly to the bus waveguide and interact less with any etched sidewalls. From the Q factors, we can estimate the coupling efficiency from the optical modes to the grating coupler. Resonator coupling efficiency is $1 - Q_e/Q_i$, where Q_e is extrinsic (5,300: measured directly), and Q_i is intrinsic (55k: estimated from loss measurements). Half of the viable PL propagates

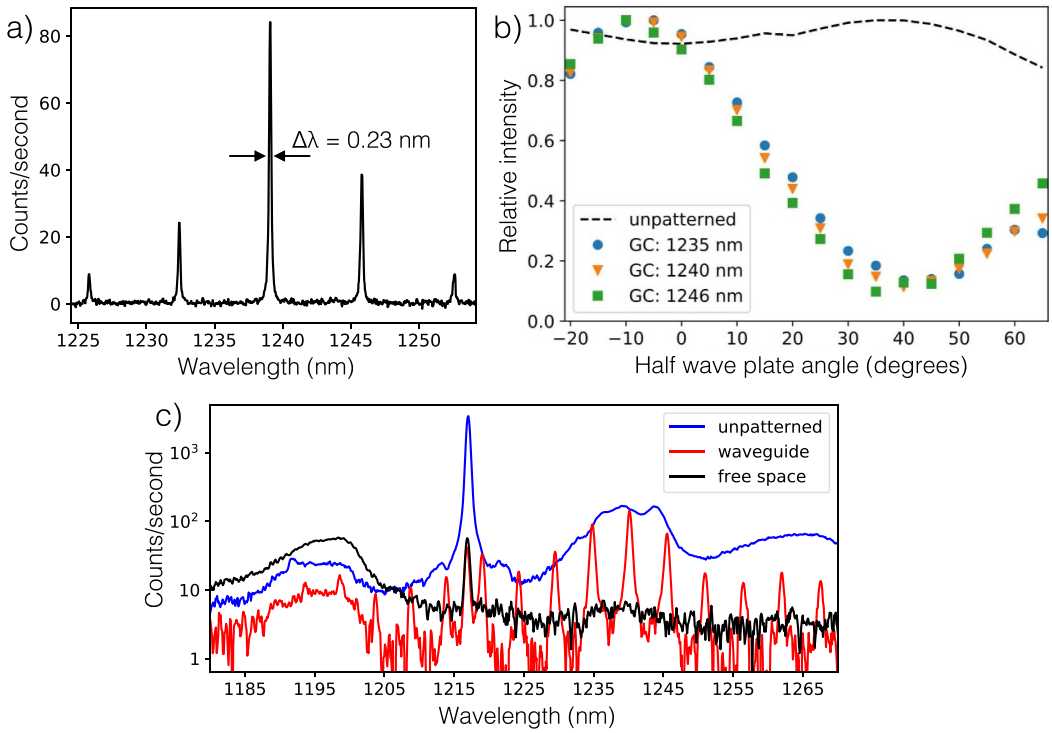

Figure 5. (a) High resolution spectrum of the sideband of the MRR with $r = 8\mu$m (figure 4(c)). The Q-factor of the central peak is at least 5,300. (b) Polarization dependence of light collected from the grating coupler (GC) compared to unpatterned control region. The GC curves are derived from three peaks of the $r = 10$ μm microring (figure 4(d)). Each curve is normalized to its maximum, and the values collected from the GC are first normalized by the corresponding unpatterned value. Note that (a) and (b) are different devices. (c) Comparison of waveguide-coupled and free-space-coupled PL from the $r = 10$ μm microring. The ZPL is visible in the free-space emission, but resonance features are not.

counter-clockwise and travels away from the GC to a waveguide taper. The waveguide from MRR and GC is 200 μm long, resulting in 0.36 dB of loss. The net efficiency between light in a cavity mode and the front of the GC is thus estimated to be 43%.

Figure 5(b) shows the PL polarization. To measure polarization, a half wave plate and polarizer were placed before the razor blade assembly. The allowed polarization angle is twice the half wave plate angle. Values labeled 'GC' refer to the amplitudes of different peaks in the waveguide-coupled sideband of the $r = 10$ μm MRR (figure 4(d)). Unpatterned values refer to the ZPL amplitude of an unpatterned control region. The degree of polarization of the GC emission was substantially stronger (88% depth) than that of the control (7.8% depth), which is corroborative because the GC is designed to direct only TE light vertically towards the objective. A half wave plate angle of zero corresponds to S-polarization (E-field perpendicular to the dichroic surface is nonzero). The sample was mounted roughly parallel to the setup such that TE polarized light in its waveguides ended up as S-polarized in the setup. The maximum of GC traces actually occurred at $-10° \pm 5°$. Most likely, this means that the sample was rotated by this amount away from parallel.

Figure 5(c) compares waveguide-coupled and free-space-coupled emission for the $r = 10$ μm MRR. In the sideband, there was no periodic resonance structure in the free-space-coupled component. This confirms that PL was not preferentially emitted into resonator modes, rather, that PL which was emitted into the modes preferentially coupled to the bus waveguide. For this radius and above, most of the pump power missed the MRR waveguide implanted with W centers and instead went through the ring center. As a result, the free-space-coupled ZPL was dimmer than the unpatterned ZPL. This contrasts with similar measurements of a microdisk in [24] wherein the microdisk was implanted throughout, and free-space emission was slightly brighter than the control.

A broad emission band appeared at 1186–1202 nm, which we believe to originate from unimplanted silicon. In this sample, the silicon slab more than 3 μm from waveguides was not etched in order to reduce electron beam write times (see figure 2(b)), which means, as an artifact of fabrication, there was an unetched, unimplanted silicon disk in the center of the MRR that was, for the large MRRs, illuminated with the majority of the pump power. This band was visible in all three traces, but its brightness relative to the ZPL increased by two orders-of-magnitude when comparing the free-space spectra between the MRR and

unpatterned control. This feature was strongly non-linear and sensitive to pump power and spot size, explaining why it is prominent here (21 mW pump) but not in most measurements above (11 mW pump). In both control and waveguide-coupled traces, it was about one order-of-magnitude dimmer than the W-center sideband; nevertheless, we can observe that this component was waveguided as evidenced by the resonances here visible at 1194 nm, 1198 nm, and 1202 nm. Luminescence features at these wavelengths have been observed from other silicon samples [10, 26] and likely originate from a diversity of broadened phonon-assisted transitions and/or other defect states [9].

5. Discussion

Previous work on waveguide-coupled W-center emission used electrical pumping and on-chip detection [14] whereas this work used free-space optical pumping and collection techniques. The integrated and free-space approaches present complementary advantages for research. As a consequence of optical pumping, a whole array of devices can be probed in a single cooldown. Luminescence properties can be studied independent of electrical properties such as ohmic heating. Finally, fabrication is two-step (Si rib etch, Si ion implant) instead of seven-step needed for electrical injection (Si rib etch, Si partial etch, Si ion implant, heavy/light boron, heavy/light phosphorus) [14]. In addition to these optical pumping advantages, optical collection provides other complementary advantages. Superconducting detectors are not required, meaning that operating temperature can be 40 K instead of 1 K. Free-space collection allows use of commercial detection instruments (e.g. spectrometers, high-speed diodes, cameras) without a need for fibers in the cryostat. The presented techniques could thus play a central role in the characterization of cryogenic silicon photonic platforms. As an example, we have observed the FSRs of various MRRs and precisely determined their group velocity by examining the sideband spectrum, while any sort of on-chip detection approach would require an on-chip spectrometer to provide similar information.

In several cases, it would be desirable to make a resonance align with the bright ZPL. This alignment presents a challenge because both the resonances and the ZPL are narrow, and the resonant wavelengths are sensitive to fabrication variability. One approach to resonance alignment are cavities designed with FSRs smaller than the ZPL linewidth, which would ensure that at least one resonance would fall within the ZPL. In this work, the $r = 30$ μm MRR has an FSR that meets the condition; however, this device is much larger than the pump spot size, so nearly all of the pump power passes through the center of the ring, missing the implanted waveguide. We fabricated a $r = 40$ μm device, but it was not measurable for this reason. Next steps could include modifying the ring shape or increasing pump power further. In general, the approach of using small-FSR cavities has the issue that they must be physically large, meaning that they have undesirably large footprint and capacitance. Additionally, without a means of tuning, parasitic index changes (e.g. from electrical pumping) cannot be countered.

Refractive index tuning is a more favorable approach for static and dynamic resonance alignment. Tuning is typically implemented with heaters at room temperature. Below 4 K, however, thermooptic tuning is likely not viable because dn/dT approaches zero [27]. There are other candidate approaches to refractive index tuning at low temperature, including carrier depletion modulation [28], electromechanical tuning [29], and localizing heating to raise the device temperature to between 4 K and 40 K. Static adjustment of MRR resonances could be realized with defect-mediated or other postfabrication trimming [30–32], although these techniques are not capable of dynamic adjustment.

Investigations into a W-center laser would be of particular interest for further work. We did not observe conclusive evidence of lasing in this study primarily due to the resonance alignment challenge. A silicon laser would have a variety of applications for on-chip optical measurement and non-linear optics, for example, photon pair generation through degenerate four wave mixing [33, 34]. Stimulated emission has been observed from G-center defects in nanopatterned silicon [35]. It remains to be shown whether population inversion—let alone amplification—can be achieved in a waveguide that is implanted with W centers.

Substantial research has been dedicated to study of PL in photonic crystal cavities, which differ significantly from MRR cavities [36–38]. Photonic crystal cavity designs often have a goal of minimizing mode volume, while MRRs make use of their small FSRs to more easily align a cavity resonance to the emitter wavelength. Their FSRs are inversely proportional to their mode volumes, which are the product of circumference and modal cross-section. MRRs are essentially bent waveguides that can be oxide-clad. As compared to air-clad photonic crystals, MRRs integrate more readily with traditional silicon photonic platforms, metal layers for index tuning, and other waveguide-based photonic integrated circuits.

The data in this manuscript might be improved by characterizing the GC response spectrum, but likely only slightly. As seen in figure 2(c) and (d), emission appeared to originate entirely from the front of the GC, and sometimes the emission pattern was bifurcated into two lobes, which indicates that this GC is not optimal. Despite the GC being non-optimal, its response is flat over the phonon sideband of interest, which

can be inferred by comparing the shape of the control spectrum to the envelope of GC peaks in figure 4. The current setup would be ideal for GC characterization and optimization in further work: using an array of identical sources coupled to varying GCs, the GC that is optimal for objective-coupled normal emission at 1218 nm at 20 K could be found in a single cooldown.

This work presents several other directions for further study. Optical cavities provide a degree of control over emitter lifetime, as in reference [20]. Source lifetime is a critical parameter for superconducting optoelectronic neural networks [39]. Other silicon defect centers can be induced by lithium, carbon, or copper implants [9]. We find that, in practice, W centers produced by silicon ion implant have been more reliable in terms of brightness uniformity. These other centers possess complementary advantages, and further work could apply the current techniques to their investigation. Another prospective direction would be using the broad sideband for wavelength-division multiplexed (WDM) sources. Although the ZPL peak is 21-times brighter than the peak of the sideband, the sideband contains 55% of total emission power when integrated from 1230 nm to 1275 nm. This power may prove sufficient to implement multiwavelength neuromorphic silicon photonic architectures [40] with monolithically integrated light sources. Finally, engineering W-center density to be on the order of λ^{-3} (one emitter per wavelength volume) could be a route to silicon single-photon sources; however, at this time, the density of W centers has not been measured, let alone as a function of implant parameters.

In conclusion, we have used micro-PL measurements with a spatial-filtering technique to unambiguously measure microcavity- and waveguide-coupled luminescence from silicon light sources. These all-silicon sources were locally created with lithographic patterning and integrated with photonic circuits. We found that light emitted into resonant modes is preferentially coupled to an adjacent waveguide. We have illustrated how this setup can employ the phonon sideband as a tool to characterize cryogenic silicon photonic circuits, extracting device values for FSR, group velocity, quality factor, and polarization. These results and methods open numerous directions for further research of fundamental defect center properties, all-silicon active devices, and large-scale photonic information processing.

We thank R. Boutelle and K. Silverman for helpful discussions on the experimental setup. We thank S.-P. Yu and N. Sanford for editorial input. This is a contribution of NIST, an agency of the U.S. Government, not subject to copyright.

ORCID iDs

A N Tait https://orcid.org/0000-0002-9774-4131
S M Buckley https://orcid.org/0000-0003-2809-9287
A N McCaughan https://orcid.org/0000-0002-8553-6474
S Papa Rao https://orcid.org/0000-0002-5893-2535
S W Nam https://orcid.org/0000-0002-4472-4655
J M Shainline https://orcid.org/0000-0002-6102-5880

References

[1] Pérez D, Gasulla I and Capmany J 2018 *Opt. Express* **26** 27265–78
[2] Shainline J M, Buckley S M, Mirin R P and Nam S W 2017 *Phys. Rev. Applied* **7** 034013
[3] Tait A N, de Lima T F, Zhou E, Wu A X, Nahmias M A, Shastri B J and Prucnal P R 2017 *Sci. Rep.* **7** 7430
[4] Liang D and Bowers J E 2010 *Nat. Photon.* **4** 511–17
[5] Zhou Z, Yin B and Michel J 2015 *Light: Sci. Appl.* **4** e358–e358
[6] Roelkens G, Liu L, Liang D, Jones R, Fang A, Koch B and Bowers J 2010 *Laser Photon. Rev.* **4** 751–79
[7] Liao M, Chen S, Park J S, Seeds A and Liu H 2018 *Semicond. Sci. Technol.* **33** 123002
[8] Bao S *et al* 2017 *Nat. Commun.* **8** 1845
[9] Davies G 1989 *Phys. Rep.* **176** 83–188
[10] Shainline J and Xu J 2007 *Laser Photon. Rev.* **1** 334–48
[11] Brádler K, Dallaire-Demers P L, Rebentrost P, Su D and Weedbrook C 2018 *Phys. Rev.* A **98** 032310
[12] Tan S H and Rohde P P 2019 *Rev. Phys.* **4** 100030
[13] Davies G, Lightowlers E C and Ciechanowska Z E 1987 *J. Phys. C: Solid State Phys.* **20** 191–205
[14] Buckley S, Chiles J, McCaughan A N, Moody G, Silverman K L, Stevens M J, Mirin R P, Nam S W and Shainline J M 2017 *Appl. Phys. Lett.* **111** 141101
[15] Bao J, Charnvanichborikarn S, Yang Y, Tabbal M, Shin B, Wong-Leung J, Williams J S, Aziz M J and Capasso F 2008 Point defect engineered Si sub-bandgap light-emitting diodes *Device and Process Technologies for Microelectronics, MEMS, Photonics, and Nanotechnology IV* vol 6800 ed Tan H H *et al* (Bellingham, WA: SPIE) pp 164–71
[16] Chong W, Yu Y, Yang R D, Liang L, Fei X and Ji-Ming B 2011 *Chinese Phys.* B **20** 026802
[17] Buckley S M, Tait A N, Moody G, Olson S, Herman J, Silverman K L, Rao S P, Nam S W, Mirin R P and Shainline J M 2019 arXiv: 1911.01317
[18] Radulaski M *et al* 2015 *ACS Photonics* **2** 14–9
[19] Shakoor A *et al* 2013 *Laser Photon. Rev.* **7** 114–21
[20] Sumikura H, Kuramochi E, Taniyama H and Notomi M 2014 *Sci. Rep.* **4** 5040

[21] Koseki S, Zhang B, De Greve K and Yamamoto Y 2009 *Appl. Phys. Lett.* **94** 051110
[22] Englund D, Ellis B, Edwards E, Sarmiento T, Harris J S, Miller D A B and Vučković J 2009 *Opt. Express* **17** 15409–19
[23] Coles R J, Prtljaga N, Royall B, Luxmoore I J, Fox A M and Skolnick M S 2014 *Opt. Express* **22** 2376–85
[24] Tait A N, Buckley S M, McCaughan A N, Chiles J T, Nam S, Mirin R P and Shainline J M 2020 Microresonator-enhanced, waveguide-coupled emission from silicon defect centers for superconducting optoelectronic networks *IEEE Optical Fiber Comm. Conf. (OFC)* (https://doi.org/10.1364/OFC.2020.M2K.6)
[25] Lu Z, Jhoja J, Klein J, Wang X, Liu A, Flueckiger J, Pond J and Chrostowski L 2017 *Opt. Express* **25** 9712–33
[26] Lightowlers E C, Canham L T, Davies G, Thewalt M L W and Watkins S P 1984 *Phys. Rev.* B **29** 4517–23
[27] Komma J, Schwarz C, Hofmann G, Heinert D and Nawrodt R 2012 *Appl. Phys. Lett.* **101** 041905
[28] Gehl M *et al* 2017 *Optica* **4** 374–82
[29] Yan X, Wu J, Watt R C, Nantel M K T, Chrostowski L and Young J F 2018 Mechanically tunable photonic crystal cavity with high quality factor and small mode *Conf. on Lasers and Electro-Optics* (San Jose, CA: Optical Society of America) p JTh2A.3
[30] Ackert J J, Doylend J K, Logan D F, Jessop P E, Vafaei R, Chrostowski L and Knights A P 2011 *Opt. Express* **19** 11969–76
[31] Alipour P, Atabaki A H, Askari M, Adibi A and Eftekhar A A 2015 *Opt. Lett.* **40** 4476–9
[32] Chen B, Yu X, Chen X, Milosevic M M, Thomson D J, Khokhar A Z, Saito S, Muskens O L and Reed G T 2018 *Opt. Express* **26** 24953–63
[33] Gentry C M *et al* 2015 *Optica* **2** 1065–71
[34] Savanier M, Kumar R and Mookherjea S 2016 *Opt. Express* **24** 3313–28
[35] Cloutier S G, Kossyrev P A and Xu J 2005 *Nat. Mater.* **4** 887–91
[36] Akahane Y, Asano T, Song B S and Noda S 2005 *Opt. Express* **13** 1202–14
[37] Kassa-Baghdouche L 2019 *Phys. Scr.* **95** 015502
[38] Kassa-Baghdouche L and Cassan E 2018 *Photon. Nanostruct. - Fundamentals Appl.* **28** 32–6
[39] Shainline J M *et al* 2019 *J. Appl. Phys.* **126** 044902
[40] Tait A N, Nahmias M A, Shastri B J and Prucnal P R 2014 *J. Lightwave Technol.* **32** 3427–39